Assessments of a Turbulence Model based on Menter's Modification to Rotta's Two-Equation Model

Khaled S. Abdol-Hamid [1]
NASA Langley Research Center, Hampton, Virginia 23693

The main objective of this paper is to construct a turbulence model with a more reliable second equation simulating length scale. In the present paper, we assess the length scale equation based on Menter's modification to Rotta's two-equation model. Rotta shows that a reliable second equation can be formed in an exact transport equation from the turbulent length scale L and kinetic energy. Rotta's equation is well suited for a term-by-term modeling and shows some interesting features compared to other approaches. The most important difference is that the formulation leads to a natural inclusion of higher order velocity derivatives into the source terms of the scale equation, which has the potential to enhance the capability of Reynolds-averaged Navier-Stokes (RANS) to simulate unsteady flows. The model is implemented in the PAB3D solver with complete formulation, usage methodology, and validation examples to demonstrate its capabilities. The detailed studies include grid convergence. Near-wall and shear flows cases are documented and compared with experimental and Large Eddy Simulation (LES) data. The results from this formulation are as good or better than the well-known SST turbulence model and much better than k-ε results. Overall, the study provides useful insights into the model capability in predicting attached and separated flows.

Nomenclature

2-D	=	*two-dimensional*
C_f	=	skin friction coefficient
C_p	=	pressure coefficient
$C_{\phi 1}$	=	Production coefficient for the second equation
$C_{\phi 2}$	=	Dissipation coefficient for the second equation
$C\mu$	=	turbulence viscosity coefficient
Dj	=	Diameter of nozzle exit
f_c	=	compressibility function
k	=	turbulence kinetic energy
L	=	turbulence length scale
$L_{\upsilon k}$	=	von Karman length scale
P_k	=	turbulence production
U	=	velocity
SST	=	Shear Stress Turbulence model
u+	=	inner wall variable for streamwise velocity
y+	=	inner wall variable for distance
ε	=	turbulence dissipation
Φ	=	second turbulence equation variable
σ_k	=	diffusion coefficient for first equation
σ_Φ	=	diffusion coefficient for second equation
κ	=	von Karman constant

[1] Research Aerospace Engineer, Configuration Aerodynamics Branch, MS 499, AIAA Associate Fellow

μ_l = laminar viscosity
μ_t = turbulence viscosity
ρ = density
$\zeta_1 \zeta_2 \zeta_3$ = constants for the second turbulence equation

I. Introduction

While two-equation models have been used routinely for the last 50 years, they are based on kinetic energy equation and either dissipation or time-scale equation to evaluate length scale. These two scales are obtained from the solution of two presumable independent transport equations, like the k-ε or k-ω model or any other formulations that uses k equation. The mechanism of the second equation for determining turbulent length scale is not fully understood and a number of formulations use a special boundary condition for simulating wall boundary condition. Even the more complex model closures like Reynolds Stress models (RSM), or Explicit Algebraic Reynolds Stress model (EARSM) are still using length scale equation based on an underlying two-equation model. Almost all two-equation models use the turbulent kinetic energy, k, and its transport equation as one of the primary variables. The exact transport equation for k can be modeled with few relatively straightforward assumptions.

Historically, the modeling of the second equation is therefore purely heuristic, using dimensional arguments [1]. These models are only using strain-rate or vorticity derived from the mean flow resulted in only one scale from the equilibrium of source terms for both equations. In fact, the second equation is considered, in most cases, the weakest link in using turbulence models including much more complex approaches such as full Reynolds stress and hybrid RANS/LES formulations. It is very difficult to justify using any of the complex turbulence models without fixing or using a better form for the second equation. The main objective of the present paper is to assess a better form of the second equation. One of limited exceptions is the modeling concept proposed by Rotta [1], which can be formed in an exact transport equation for the turbulent length scale. *L*. Rotta's equation is well suited for a term-by-term modeling and shows some interesting features compared to other approaches. The most important difference is that the formulation leads to a natural inclusion of higher order velocity derivatives into the source terms of the scale equation.

In the present paper, three turbulence models based on Rotta's k-kL two-equation model are implemented in the Computational Fluid Dynamics (CFD) solver. The formulations, usage methodology, and validation examples are presented to demonstrate the enhancement of PAB3D's turbulence modeling capabilities. These models are based on the suggestion made by Menter et. al. [3-5] to replace problematic third velocity derivatives in the second equation with second velocity derivatives. This provides proper RANS performance in stable flow regions and allows the break-up of large turbulent structures for unstable flow regimes (for example, cylinder in cross flow, flow in cavities, …). Solutions from these models are compared with other forms of Reynolds-averaged Navier–Stokes results and experimental data for different flows. We will also investigate the influence of some closure terms in the predictions of these models.

To report the detailed studies including grid convergence, we will only present the results from the two-equation k-kL. Results for all near-wall and shear flows, which are reported below, have been calculated using the structured multiblock grids, resolving the viscous sublayer with $y+<1$. All simulations have been carried out on highly refined grids, avoiding any grid refinement uncertainties. The results are compared with other turbulence models and available experimental or theoretical data. Most of the cases are taken from the cases compiled in the turbulence modeling resource page [6]. The purpose of this site is to provide a central location where RANS turbulence models are documented. Here is the list of validation cases that will be discussed in detail in the paper:

A. 2D zero pressure gradient flat plate [6] will be compared with data from [6].
B. 2D backward facing step [6] will be compared with data from [7].
C. Flow over a hump model [8] will be compared with data from [8-10]
D. Axisymmetric subsonic jet [6] will be compared with experimental data from [11].
E. 2-D curved backward facing Step [6] will be compared with LES data from [12].
F. 2D periodic hill [6] will be compared with LES data from [12]

All the results show grid convergence and independent solutions. Only the backward step cases shows unsteady behavior at the medium and fine grid level. Some of the results are compared with data for PAB3D [13] and CFL3D [14] CFD codes. In all the comparisons, the results from these codes are computed at the fine grid level. In general, the results are as good as or better than the SST turbulence model compared with available data.

II. Turbulence models

The three turbulence models, listed here, are based on the approach made by Menter [3-5]. For high-speed flow, the compressibility correction function has been added. A complete list of coefficients used by all three models has been defined. The first model is based on Rotta's k-kL (Φ =kL) with modification made by Menter by replacing velocity third derivative with a second derivative. The second model is based on transforming the kL equation to a $\sqrt{kL}$ formulation, which represents turbulent viscosity. The third model is based on one-equation, solving only the second equation and evaluates k with the assumption that production equals dissipation. The three models are casted in k-Φ form as follows:

$$\frac{\partial \rho k}{\partial t} + \frac{\partial \rho U_j k}{\partial x_j} = \left[P_k + \frac{\partial}{\partial x_j}\left(\mu_l + \frac{\mu_t}{\sigma_k}\frac{\partial k}{\partial x_j} \right) + VSM_k \right] - \left[C_\mu^{3/4} \rho \frac{k^{p1}}{\Phi}(1. + f_c) \right] \tag{1}$$

$$\frac{\partial \rho \Phi}{\partial t} + \frac{\partial \rho U_j \Phi}{\partial x_j} = \left[C_{\phi 1}\frac{\Phi}{k} P_k + \frac{\partial}{\partial x_j}\left(\mu_l + \frac{\mu_t}{\sigma_\Phi}\frac{\partial \Phi}{\partial x_j} \right) + VSM_\Phi \right] - C_{\phi 2}\rho k^{p1-1} \tag{2}$$

Where,

$$C_{\phi 1} = \left(\zeta_1 - \zeta_2 \left(\frac{L}{L_{\upsilon k}} \right)^2 \right)$$

$$C_{\phi 2} = (\zeta_3 + p_1 C_\mu^{3/4} f_c)$$

$$C\mu = 0.09 \tag{3}$$

The kinetic energy production is modeled as:

$$P_k = -u_i u_j \frac{\partial u_i}{\partial x_j}$$

$$\mu_t = C_\mu^{1/4} \frac{\rho \Phi}{k^{p1-1.5}} \tag{4}$$

The von Karman length scale, $L_{\upsilon k}$, is defined as:

$$L_{\upsilon k} = \kappa \left| \frac{U'}{U''} \right| \tag{5}$$

Where,

$$U' = S = \sqrt{2 S_{ij} S_{ij}}$$

$$S_{ij} = \frac{1}{2}\left(\frac{\partial U_i}{\partial x_j} + \frac{\partial U_j}{\partial x_i} \right)$$

$$U'' = \sqrt{\left(\frac{\partial^2 U_i}{\partial x_k^2} \frac{\partial^2 U_i}{\partial x_j^2} \right)}$$

To avoid overly large or small values of the length scale ratio, $L/L_{\upsilon k}$, we set $L/C_{l1} < L_{\upsilon k} < C_{l2}\kappa d$, where d is the distance from the nearest wall and C_{l1} =10 and C_{l2} =1.3. The upper limit in von Karman length scale is based on attached flow assumption that it is directly proportion to distance from the wall. This assumption is not true for separated flow. We are proposing to reduce the upper limit in the separation region using production (P) to dissipation (ε) ratio as:

$$L/C_{l1} < L_{\upsilon k} < C_{l2}\kappa d\left[P/C_\mu^{3/4}\rho\frac{k^{p1}}{\Phi} \right] \tag{6}$$

The length scale, L, is calculated from the following equation:

$$L = \frac{\Phi}{k^{p1-1.5}}$$

To integrate the model through the viscous sub-layer, additional near wall damping terms are required. The following *VSM* terms are added to the right hand sides of the *k* and the ϕ equation, respectively (VSM):

$$VSM_k = -2\mu_l \frac{k}{d^2}$$
$$VSM_\Phi = -6\mu_l \frac{\Phi}{d^2} f_\Phi \tag{7}$$

Where,

$$f_\Phi = \frac{1 + C_{dl}\xi}{1 + \xi^4}$$
$$\xi = \frac{\sqrt{0.3k}d}{20\nu_l}$$

To close the turbulence model, reference [3] used the following logarithmic requirements:

$$\frac{dU}{dy} = \frac{u_\tau}{\kappa y}$$
$$k = \frac{u_\tau^2}{C_\mu^{1/2}}$$
$$L = \kappa y$$
$$\nu_t = u_\tau \kappa y$$

Then,

$$\zeta_2 = \zeta_1 - \zeta_3 \frac{1}{C_\mu^{3/4}} + \frac{\kappa^2}{\sigma_\phi C_\mu^{1/2}}$$

(8)

The final set of constants and coefficients for the $k-\sqrt{k}L$ turbulence model as listed from reference [3]:

$$\begin{aligned}
&\text{for} \quad \Phi = \sqrt{k}L \\
&pl = 2 \\
&\zeta_1 = 0.8 \\
&\zeta_2 = 1.47 \\
&\zeta_3 = 0.0288 \\
&\sigma_k = 2/3 \\
&\sigma_\Phi = 2/3
\end{aligned} \tag{9}$$

To come up with the present set of constants and coefficients for the present $k-kL$:

a) using the logarithmic requirements
b) limit the range for $1.1 < \zeta_1 < 1.3 \;\; 0.95 < \zeta_2 < 1.0$ as suggested by Rotta [2]
c) Calibrate both coefficients for the best results for cases A and D from the present paper.

Below is the final list of constants and coefficients used in the present paper for $k-kL$ turbulence model:

$$\begin{aligned}
&\text{for} \quad \Phi = kL \\
&pl = 2.5 \\
&\zeta_1 = 1.2 \\
&\zeta_2 = 0.97 \\
&\zeta_3 = 0.13 \\
&\sigma_k = 1.0 \\
&\sigma_\Phi = 1.0
\end{aligned} \tag{10}$$

<u>One-equation</u>

The current model k-$\sqrt{k}L$ formulation is well suited for the transformation to a one-equation model considering

$$\frac{\partial \rho \Phi}{\partial t} + \frac{\partial \rho U_j \Phi}{\partial x_j} = \left[C_{\varphi 1} \frac{\Phi}{\tilde{k}} P_k + \frac{\partial}{\partial x_j}\left(\mu_l + \frac{\mu_t}{\sigma_\Phi} \frac{\partial \Phi}{\partial x_j} \right) + VSM_\Phi \right] - C_{\varphi 2} \rho \tilde{k}^{pl-1} \tag{11}$$

Where constants for this model are same as (9) above. Assuming equilibrium between production and dissipation, turbulent kinetic energy is calculated as follow:

$$P_k = C_\mu^{3/4}\rho\frac{\tilde{k}^2}{\Phi}$$

$$\tilde{k} = \sqrt{\frac{\mu_t S}{\rho C_\mu^{1/2}}} \qquad (12)$$

III. Results and Discussions

A. 2D Zero Pressure Gradient Flat Plate Case

Figure 1 shows the sketch of the flat plate test case with boundary conditions used in this analysis. This is a subsonic M = 0.2 case at Re = 5 million based on unit length. The following plot in Figure 2 shows the convergence of the wall skin friction coefficient at x=0.97 using five levels of grid size with k-kL turbulence model. Each coarser grid is exactly every-other-point of the next finer grid, ranging from the super fine grid of 544x384 cells to the very coarse grid of 34x24 cells. In the plot, the x-axis is plotting $(1/N)^{1/2}$, which is proportional to grid spacing (h). At the left of the plot, h=0 represents an infinitely fine grid. The difference between the coarsest and finest grid is less than 0.0003 in skin friction. Only, the very coarse grid is out of order from the other levels. The surface skin friction coefficient, using the k-kL turbulence model on the finest 544 x 384 grid cells over the entire plate, varies with respect to momentum thickness Reynolds Number, as shown in Figure 3. The k-kL results are in good comparisons with the SST solution computed using CFL3D code [6].

Figure 4 shows the grid effects in predicting u+ using coarse, medium, fine and super fine grids. All the grid levels predict similar u+ variations with y+ except for the coarse grid that slightly under predicted these variations. Using the finest grid results, the variation of u+ velocity with respect to y+ predicted using k-kL, SST, and k-ε turbulence models is shown in Figure 5. The k-kL results are in very good comparisons with SST and Coles data taken from Ref. [6]. The k-ε results, as expected, largely under predicted the u+ levels through the entire y+ range that is caused by predicting much higher surface skin friction than k-kL or SST models.

Turbulence kinetic energy and viscosity are other quantities used to validate the quality of turbulence model predictions. Figure 6 shows the grid convergence in the prediction of the kinetic energy values at x=0.97. Only the coarse grid shows larger values of turbulence kinetic energy up to Z=0.01. The medium, fine, and superfine grid levels predicted very similar turbulence kinetic energy distribution. Figure 7 shows comparisons between of the predicted turbulence kinetic energy using k-kL, SST, and k-ε turbulence models. The k-kL and SST results are in very good agreement, however, the k-ε results show much higher turbulence kinetic energy than either of the other two models. Figure 8 shows the grid convergence in the prediction of turbulence viscosity. Similar to the observation made for the kinetic energy, the coarse grid predicted much higher turbulence viscosity than other grids. This is caused by the fact that the coarse grid has less than 50 cells in the normal direction and less than 25 cells to capture the entire boundary layer.

B. 2D Backward Facing Step Case

The 2D backward facing step case is a backward step flow case with a sharp corner. A series of 2-D grids, nondimensionalized by the step height H, are used in this analysis taken from Ref. 6. As structured grids, these are comprised of 4 zones, connected in a one-to-one fashion. Each coarser grid is exactly every-other-point of the next finer grid, ranging from the finest of 256 x 256, 96 x 256, 384 x 448, and 128x448 cells to the coarsest 64 x 64, 24 x 64, 96 x 112, and 32 x 112 cells. Figure 9 shows a portion of the coarse grid distribution. In this case, a turbulent boundary layer encounters a sudden back step, causing flow separation. The flow then reattaches and recovers downstream of the step. The Reynolds number based on boundary layer momentum thickness prior to the step is 5000. This corresponds to a Reynolds number of approximately 36,000 based on step height H. The boundary layer thickness prior to the step is approximately 1.5H. The flow conditions for this case are:

M=0.128, Re= 36,000 (based on step height H), T=537 °R

One of the key measures of success for this flowfield of turbulence models is the prediction of separation and reattachment points downstream of the step. In the experiment [7], this was determined by laser oil-flow interferometer measurements of skin-friction and interpolation of the zero skin-friction location. The experimental reattachment point is around 6.26 +/- 0.1. The U_{ref} is the reference velocity at the center-channel near x/H=-4 (where H=1 grid unit). The coarse grid solution using the k-kL model is steady, where the other two grid levels are showing unsteady behavior as shown later in Figure 12. The time-average of the unsteady data for all cases is used to compare with experimental data. Next, we evaluate the correction made for the upper limit of von Karmen length scale (equation 6), referred to as the modified k-kL model. Figure 10 shows the comparison in predicting the velocity distribution at different x/H locations using the original and modified k-kL models. There is no significant difference between the prediction using both models with exception of the velocity distribution at x/H=1. The skin friction results in Figure 11 shows more significant differences between the predictions from both models. In the region of attached flow up to x/H=2, there is no difference between both models as production to dissipation ratio is around 1.0 in the attached flow region. In the separated flow region, the ratio is much smaller than 1, which causes significant difference in prediction of skin friction. The original model is clearly under predicting the skin friction in the separated flow region and over predicts the skin friction in the region downstream the reattachment point. The modified k-kL model results are in very good agreement with experimental data.

Figure 12 (a, b and c) shows the time-averaged streamline results from the coarse, medium, and fine grid solutions. All solutions show two bubbles, one close to the corner of the step where the flow starts to separate and the other that contains the large separation bubble. The coarse grid produces a smaller first bubble and larger second bubble with reattachment location around x/H=6.78. The medium and fine grids produce very similar bubbles sizes and reattachment location is predicted at x/H=6.3 as shown in Figure 13.

Figure 13 shows the comparisons between skin friction predictions using coarse, medium and fine grids. The medium and fine grid simulations are in good agreement with experimental data in predicting the separation and reattachment locations. Figure 14 shows the skin friction comparisons between experimental data and k-kL, SST and k-ε simulations. The k-ε simulation predicts early separation and re-attachment location around x/H=5.4 compared with experimental data of 6.26. The k-kL is slightly better than SST in predicting skin friction and re-attachment point prediction. Figure 15 shows the velocity distribution comparisons between experimental data, and k-kL and SST simulations. The SST match the experimental data better at x/H=1 comparing with k-kL simulation. However, the k-kL is in closer agreement with experimental data for x/H= 6 and 10 locations.

C. 2D Hump Case

This is case 3 from the CFD 2004 validation workshop for Synthetic Jets and Turbulent Separation Control [8]. Case 3 is a Wall-mounted Glauert-Goldschmied type body, geometrically similar to that employed by Seifert & Pack [8]. The model itself is 23 inches wide between the endplates at both sides (each endplate is approximately 9.25 inches high, 34 inches long, and 0.5 inches thick with an elliptical-shaped leading edge). The model is 2.116 inches high at its maximum thickness point. In the present paper, we simulate the (baseline) case with flow conditions of M = 0.1 and Reynolds number approximately 1 million per chord. Only surface pressure and skin friction are compared with results from turbulence model simulations. Three grid levels are utilized to assist grid convergence with finest grid consisted of two zones 416x216 and 416x216 cells and the coarsest have 104x54 and 104x54 cells. This is based on structured 2D grid #5 from ref [8] as it is built with the top wall shape adjusted to approximately account for side plate blockage. Figure 16 shows a portion of the coarse grid distribution. In this case, the boundary layer is subjected to a favorable pressure gradient over the front convex portion of the body and separates over a relatively short concave section in the aft part of the body. The flow then reattaches and recovers downstream of the hump.

Surface pressure results from the modified and original k-kL turbulence models are compared with experimental data from surface mounted pressure tap [9 & 10] as shown in Figure 17. Both models compared well with experimental data with a slight improvement using the original model at x=0.8. However, the skin friction prediction from the modified model is in pretty good agreement with experimental data as compared with original model, as seen in Figure 18. There are very large differences between the original model prediction and experimental data in the separation region. The original model predicted the correct size of the separation bubble as compared with the modified model.

Figure 19 shows that there is very small effect of grid resolution on the surface pressure distribution. The turbulence model comparisons in Figure 20 show the k-kL turbulence model is slightly better than SST and k-ε turbulence models as compared with experimental data. Figure 21 shows that there is no effect of grid resolution on the skin friction results. The turbulence model comparisons in Figure 22 show the k-kL turbulence model is better than the k-ε and SST turbulence models from the pressure recovery region aft as compared with experimental data.

D. Axisymmetric Subsonic Jet Case

The axisymmetric subsonic jet case is to validate the quality of the turbulence models prediction of experimental data for shear flows. The experiment yielded measured velocities as well as turbulence quantities downstream of the jet exit using Particle Image Velocimetry (PIV) [11]. Velocity and turbulence profiles of interest are measured at the centerline (y=0) as well as other x-locations. In the present paper, we are comparing the turbulence model results with the centerline values for velocity and turbulence data. The grid used is taken from [6] and a snapshot is shown in Figure 23. The grid is made of 3 blocks of 96x96, 60x96, and 256x224 cells. Block 1 is the interior of the nozzle, block 2 is the external flow up to the nozzle and block 3 extends from the exit of the nozzle to x/Dj=40. Dj is the diameter of the nozzle exit. Coarse, medium, and fine grid levels are used in the simulation where the coarser grid is exactly every-other-point of the next finer grid. It is important to note that this axisymmetric case is not a 2-D computation; it uses a 5^o sector with one cell and symmetric boundary conditions on each side. $M_{jet}=u_{jet}/a_{jet}=0.51$, whereas the "acoustic Mach number" u_{jet}/a_{ref} is approximately 0.5. In the experiment, the axisymmetric jet exits into quiescent (non-moving) air. However, because flow into quiescent air is difficult to achieve for some CFD codes, here the solution is computed with a very low background ambient conditions ($M_{ref}=0.01$, moving left-to-right, in the same direction as the jet).

First, we are comparing the three grid levels with the experimental data to validate the grids. Figure 24 shows the comparisons between the different grid levels using k-kL turbulence model and experimental data for the normalized centerline axial velocity. The nozzle centerline exit velocity is used to normalize the data. There is a very small difference between all grid level results. The prediction of the model is in good agreement with experimental data, however, the jet core was predicted at around 7 diameters comparing with experimental data of around 6. Also, the centerline velocity results show a slightly faster decay rate than the experimental data.

The ability of the k-kLmodel in predicting shear flow with other turbulence models is shown in Figures [25-26]. The jet core length is better predicted with the k-kL model as compared with the k-ε model as shown in Figure 25. In Figure 26, both the SST and k-ε models predicted a long core length around 10 as compared with a value of 7 predicted by the k-kL model and the experimental data of around 6. The rate of decay predicted with the SST model is clearly the fastest as compared with the other models and k-kL predicted most closely with the experimental data in comparisons. The turbulence kinetic energy comparisons between turbulence models and experimental data are shown in Figure 27. The maximum value of kinetic energy is better predicted with the k-kL model as compared with the other models. The SST model overpredicted the turbulence kinetic energy level in comparisons with the other models. All models failed to replicate the slow increase of turbulence kinetic energy for $x/Dj < 6$.

E. 2-D Curved Backward Facing Step Case

In this paper, we are also comparing turbulence models predictions with LES CFD data provided by Ref. [6]. This LES case is for 2-D separating flow over a curved backward facing step. The LES was run using an incompressible code, and has been documented in several publications listed in [15]. Some relevant information is given here, but the interested reader is referred to reference [6] for complete details.

- Upstream duct height = 8.52 H (where H = step height).
- Reynolds number (based on U_{in} and H) = 13700, where U_{in} is the center-channel inlet velocity.
- At x/H=-7.34 data is extracted from LES solution [6].

The grid used in the present study is from [6]. This a two-dimensional grid of 768x160 cells extracted from the LES 23.6 million grid cells. The grid and boundary conditions is shown in Figure 32. The purpose of this comparison is to validate the ability of the k-kL model to reproduce the LES data by enforce LES boundary condition for the inflow. The inflow boundary condition was extracted from the LES data. Skin friction comparisons between the experimental data and the coarse, medium, and fine grid simulations using the k-kL model are shown in Figure 29. The skin friction variation is small between the coarse grid and the finest grid levels. The difference is very small between the medium and fine grid. . Figure 30 shows the skin friction comparisons between experimental data, and k-kL, SST and k-ε simulations. The level of skin friction predicted using k-kL is in better agreement with LES as compared with either SST or k-e prediction. Figure 31 shows the comparison between LES and RANS turbulence model data separation and reattachment locations. In comparisons with LES data, the k-kL model predicted better separation and reattachment locations as shown in Figures 30 and 31. Separation Location, X_S/H, for LES is 0.82, for k-kL is 0.86, for SST is 0.73 and for k-ε is 1.38. Reattachment Location, X_R/H, for LES is 4.35, for k-kL is 4.73, for SST is 6.31and for k-ε is 4.08.

F. 2D Periodic Hill Case

The periodic hill data in this paper compared with the CFD data were provided by Ref. [6]. This LES case is for 2-D separating flow over periodic hills. The LES was run using an incompressible code, and has been documented in several publications listed in [16]. Some relevant information is given here, but the interested reader is referred to the above publications (ERCOFTAC website) for complete details:

- Hill crest, h = 28 mm
- Hill crests are separated by $L_x = 9h$
- Channel height $L_y = 3.035h$
- Reynolds number (based on U_b and h) = 10595
- U_b is the bulk velocity at the crest of the first hill
- The flow is periodic in the streamwise direction

The finest grid resolution used in this paper is 418x194 cells and generated by ref [6]. The grid and boundary conditions are shown in Figure 32. The purpose of this comparison is to validate the ability of the k-kL model to reproduce the LES data by enforce the LES boundary condition for the inflow. The inflow boundary condition was extracted from the LES data. Skin friction comparisons between experimental data and the coarse, medium, and fine grid simulations using the k-kL model are shown in Figure 33**.** The variation is quite large between the coarse grid and the finest grid levels. The difference is much smaller between the results using medium and fine grid. The separation bubble produced by the recent family of RANS models in better agreement with LES data as shown in Figures 34 and 35 as compared with k-ε results.

IV. Concluding Remarks

Most turbulence models use turbulence kinetic energy, which is well-behaved equation. The second equation is considered the weakest link in using turbulence models including full Reynolds stress and hybrid RANS/LES formulations. The main objective of this paper is to find a better turbulence model with a more reliable second equation. Rotta shows that a reliable second equation can be formed in an exact transport equation for the turbulent length scale, *L*. Rotta's equation is well suited for a term-by-term modeling and shows some interesting features compared to other approaches. The most important difference is that the formulation leads to a natural inclusion of higher order velocity derivatives into the source terms of the scale equation. The present paper assesses the results from a two-equation turbulence model, referred to as k-kL, and based on Menter's modification to Rotta's two-equation turbulence model.

Six test cases computed with these turbulence models have been presented, which cover an attached flow flat plat case, four separated flow cases and shear flow case. The separated flow cases are the hump, the backward facing step, the curved backward facing step and the periodic hill. The flat plat case is compared with theoretical data. The hump and backward facing step cases are compared with experimental data. The last two cases are compared with LES data. The results are compared with other turbulence models such as SST and k-ε, and

theoretical as well as experimental data. They demonstrate that the k-kL model has the ability to give results similar or better than SST results. In general, the k-kL model gives much better results than k-ε turbulence model. The size of the separation bubble (separation and re-attachment locations) is better predicted by k-kL model for the hump case and the two backward facing step cases. The skin friction is better predicted by k-kL model for these cases than other SST or k-ε turbulence models. The k-kL model also gives good agreement with the experimental data for the subsonic cold jet case as compared with the other turbulence models. For all six cases, the k-kL model gives good results as compared with other turbulence models. The next step is to evaluate the ability of this model to predict unsteady flow cases, which are a critical issue with most RANS models, and allow the extension of the present formulation to be used with hybrid RANS models. Future work will extend some of the present backward facing cases to three-dimensional as well as other simple three-dimensional cases.

References

1 Launder B.E. and Spalding, D.B., (1972), Mathematical Models of Turbulence, Academic Press, London.

2 Rotta, J. C., (1951), Statistische Theorie Nichthomogener Turbulenz, *Zeitschrift für Physik,* Vol. 129, pp. 547-572.

3 Menter, F. R. and Egorov, Y., "The Scale-Adaptive Simulation Method for Unsteady Turbulent Flow Predictions. Part 1:Theory and Model Description", Flow Turbulence Combust 85:113-138, 2010.

4 Menter, F. R. and Egorov, Y., "The Scale-Adaptive Simulation Method for Unsteady Turbulent Flow Predictions. Part 2:Application to Complex Flows", Flow Turbulence Combust 85:139-165, 2010.

5 Menter, F. R.; Egorov, Y; and Rusch, D., "Steady and Unsteady Flow Modeling Using the $k-\sqrt{kL}$ Model". Turbulence, Heat and Mass Transfer, Vol. 5.

6 http://turbmodels.larc.nasa.gov/

7 Driver, D. M. and Seegmiller, H. L., "Features of Reattaching Turbulent Shear Layer in Divergent Channel Flow," AIAA Journal, Vol. 23, No. 2, Feb 1985, pp. 163-171

8 http://cfdval2004.larc.nasa.gov/

9 Seifert, A. and Pack, L. G., "Active Flow Separation Control on Wall-Mounted Hump at High Reynolds Numbers," AIAA Journal, Vol. 40, No. 7, July 2002.

10 Greenblatt, D., Paschal, K. B., Yao, C.-S., Harris, J., Schaeffler, N. W., Washburn, A. E., "A Separation Control CFD Validation Test Case, Part 1: Baseline and Steady Suction," AIAA Journal, Vol. 44, No. 12, 2006, pp. 2820-2830.

11 Greenblatt, D., Paschal, K. B., Yao, C.-S., Harris, J., "A Separation Control CFD Validation Test Case, Part 2: Zero Efflux Oscillatory Blowing," AIAA Journal, Vol. 44, No. 12, 2006, pp. 2831-2845.

12 Bridges, J. and Brown, C., "Parametic Testing on Single Flow Hot Jet," AIAA 2004-2824, 2004.

13 http://www.asm-usa.com/PAB3D/

14 http://cfl3d.larc.nasa.gov/

15 Bentaleb, Y., Lardeau, S., and Leschziner, M. A., 2012. Large-eddy simulation of turbulent boundary layer separation from a rounded step. Journal of Turbulence 13(4), pp. 1-28.

16 http://cfd.mace.manchester.ac.uk/ercoftac/

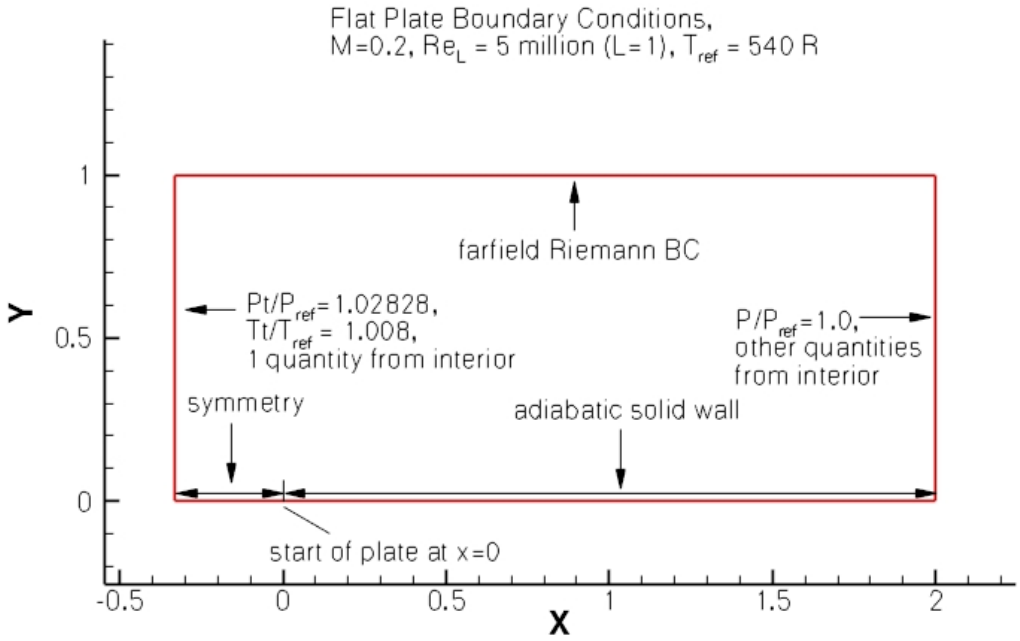

Figure 1 Sketch of M=0.2, Re=5 million flat plate test case.

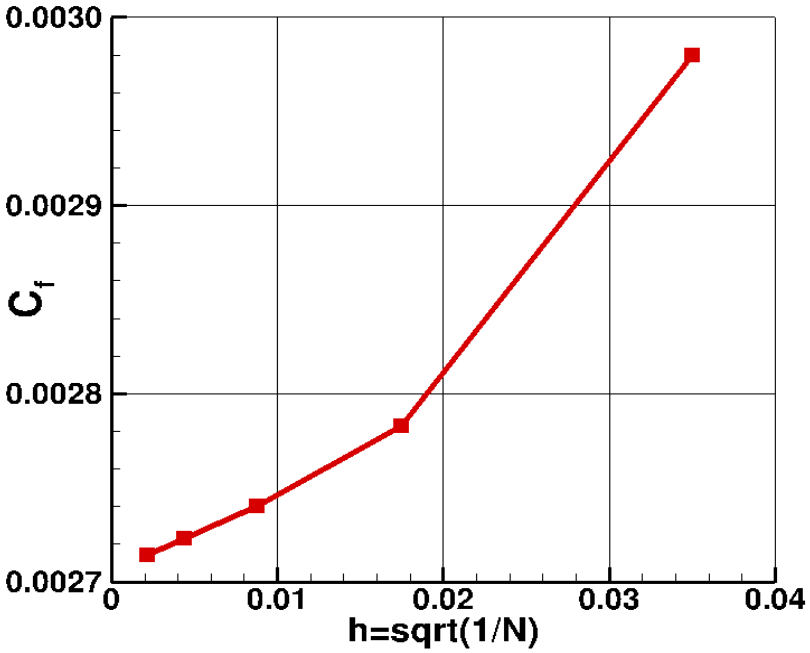

Figure 2 Skin friction coefficient variation with grid refinement using the k-kL turbulence model (PAB3D) at x=0.97.

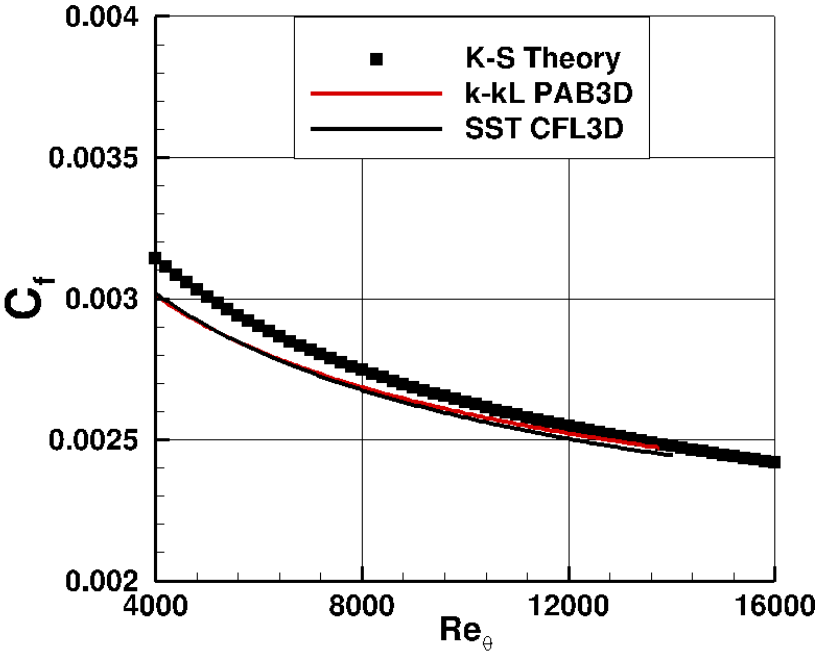

Figure 3 Flat plate skin friction coefficient variations with Re_θ showing comparisons between k-kL (PAB3D), SST (CFL3D) and K-S theory.

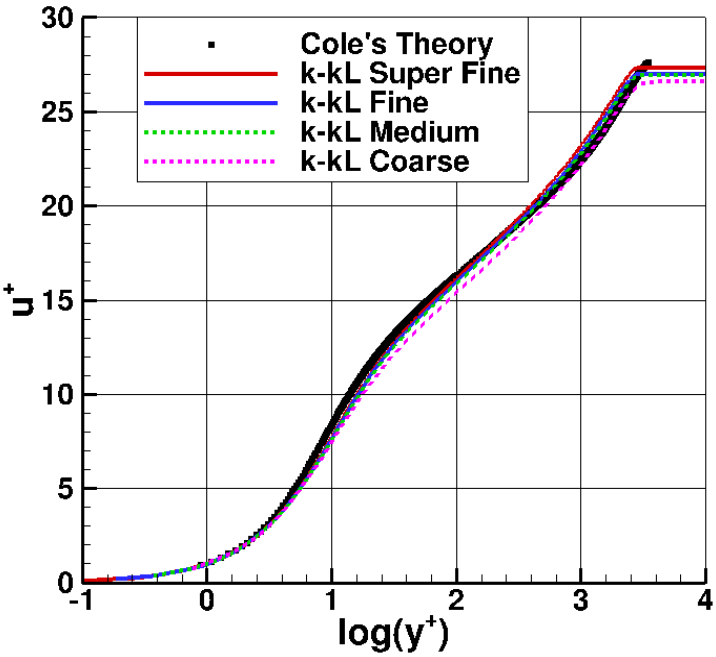

Figure 4 Flat plate u+ - y+ variations with comparisons using k-kL (PAB3D) with different grid levels and Cole's Theory at x=0.97.

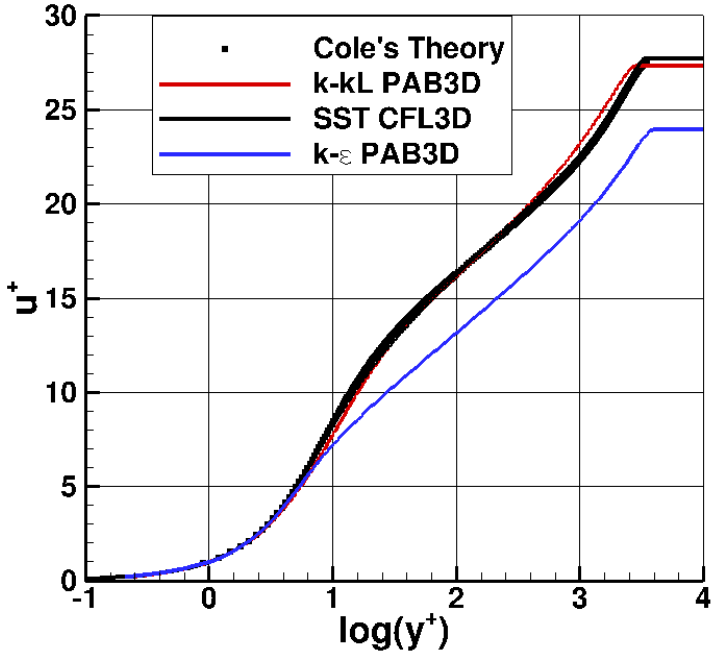

Figure 5 Flat plate u+ - y+ variations with comparisons between k-kL (PAB3D), k-ε (PAB3D), SST (CFL3D), and Cole's theory at x=0.97.

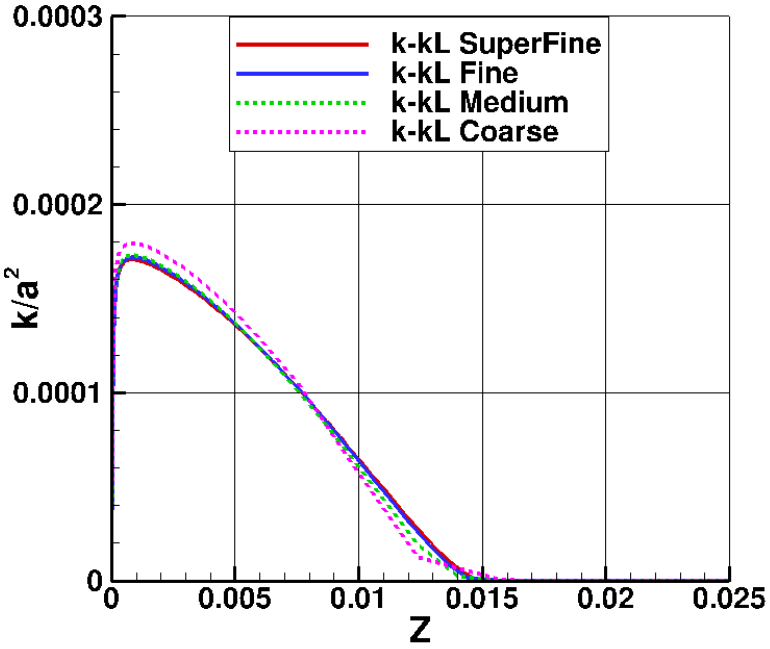

Figure 6 Flat plate k/a2 - Z variations with comparisons between k-kL (PAB3D) with different grid levels at x=0.97.

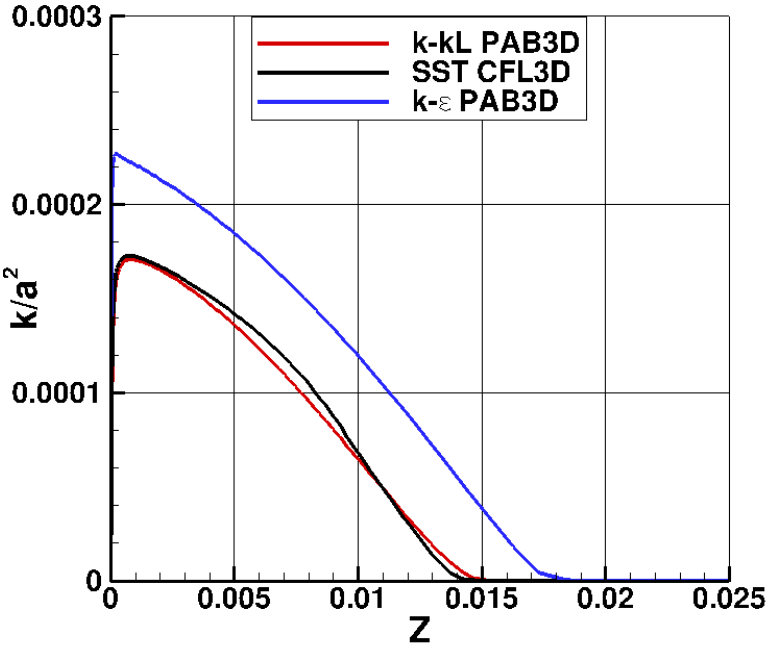

Figure 7 Flat plate k/a^2 - Z variations with comparisons between k-kL (PAB3D), k-ε (PAB3D), and SST (CFL3D) at x=0.97.

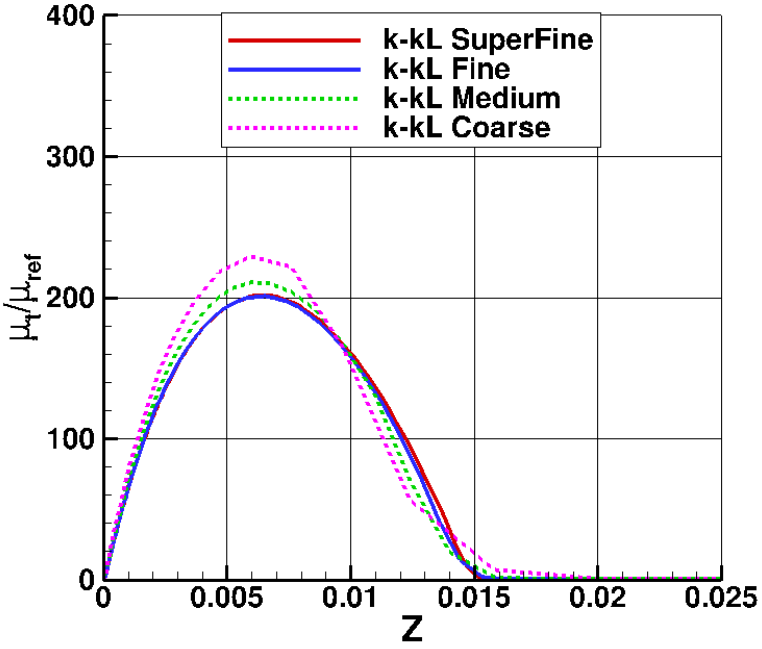

Figure 8 Flat plate turbulence viscosity - Z variations with comparisons between k-kL (PAB3D), k-ε (PAB3D), and SST (CFL3D) at x=0.97.

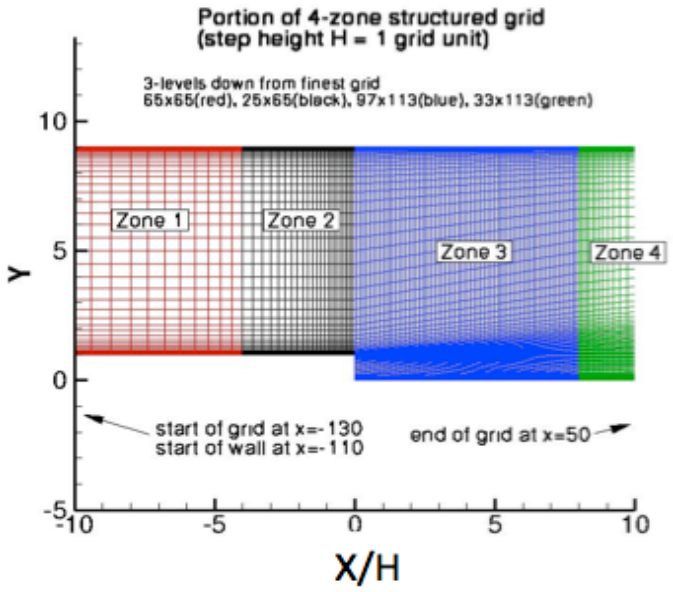

Figure 9 Grid distribution for the backward facing step grid.

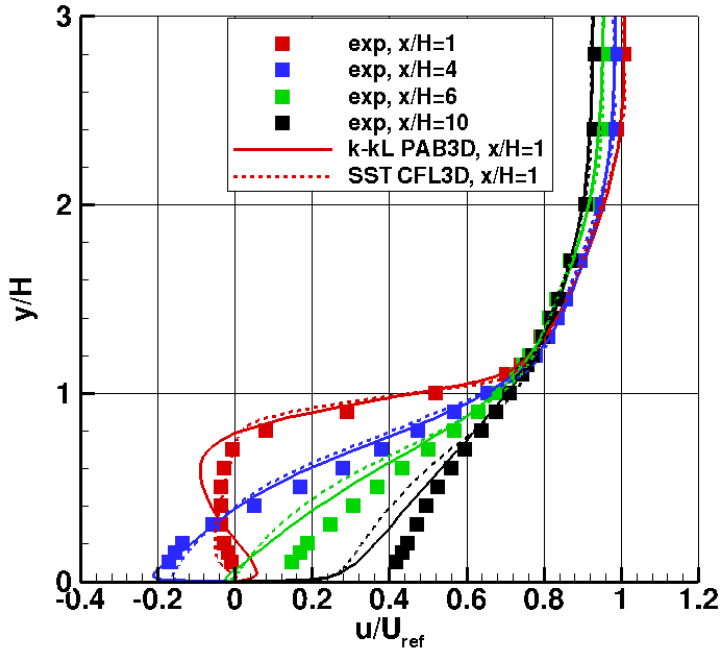

Figure 10 Velocity distribution comparisons between experimental data, and original (dashed line) and modified k-kL (solid line) predictions for backward facing step case.

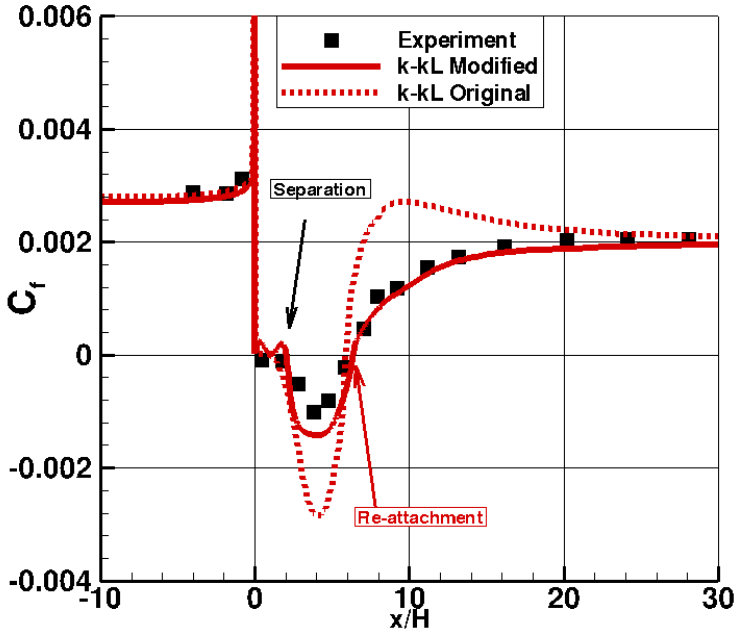

Figure 11 Skin friction comparisons between experimental data, and original and modified k-kL predictions for backward facing step case.

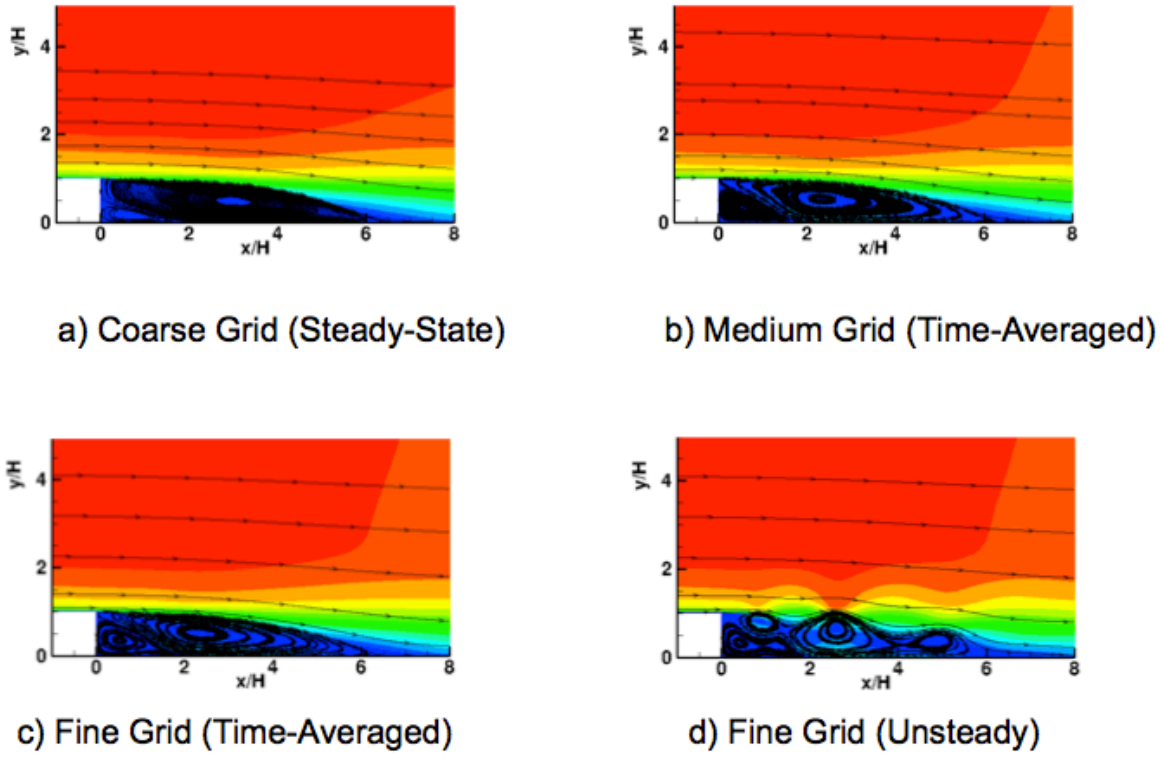

Figure 12 Streamlines predictions using k-kL turbulence model at different grid levels for backward facing step case.

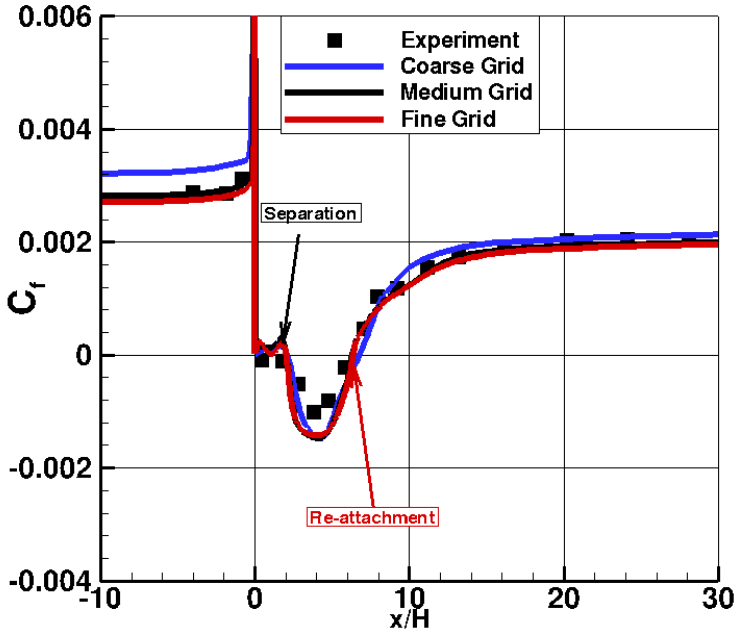

Figure 13 Skin friction comparisons between experimental data and coarse, medium, and fine grid simulations for backward facing step case.

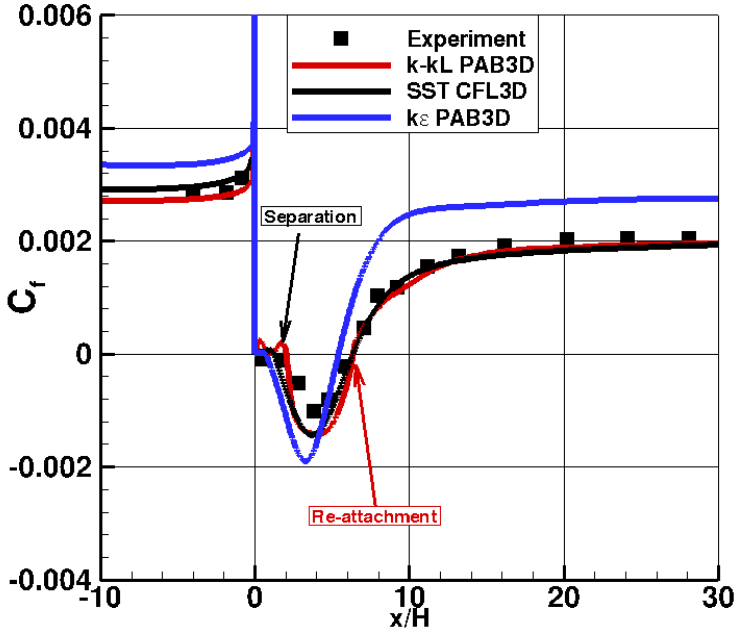

Figure 14 Skin friction comparisons between experimental data and k-kL, SST, and k-ε simulations for backward facing step case.

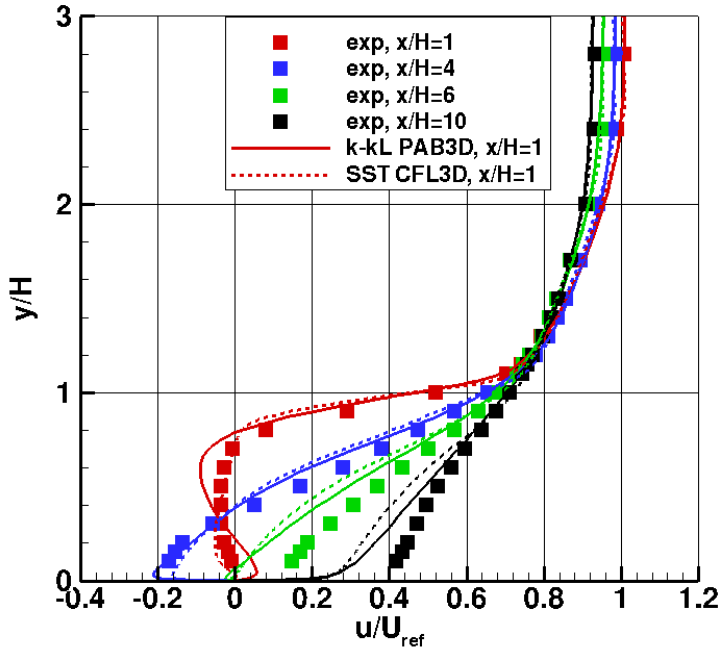

Figure 15 Velocity distribution comparisons between experimental data, and k-kL and SST simulations for backward facing step case.

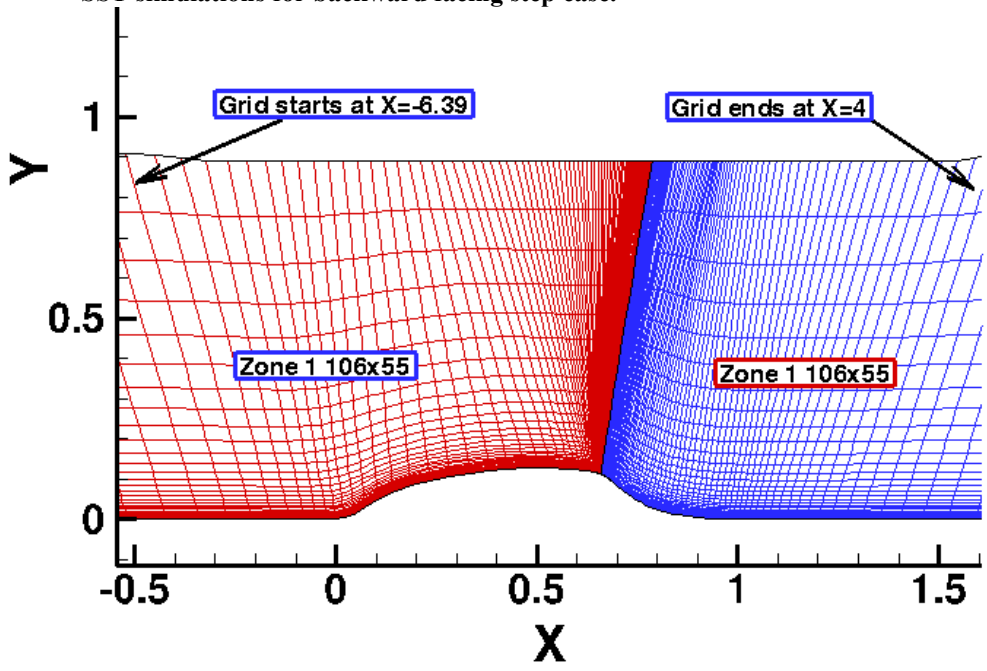

Figure 16 Grid distribution for the subsonic hump model case.

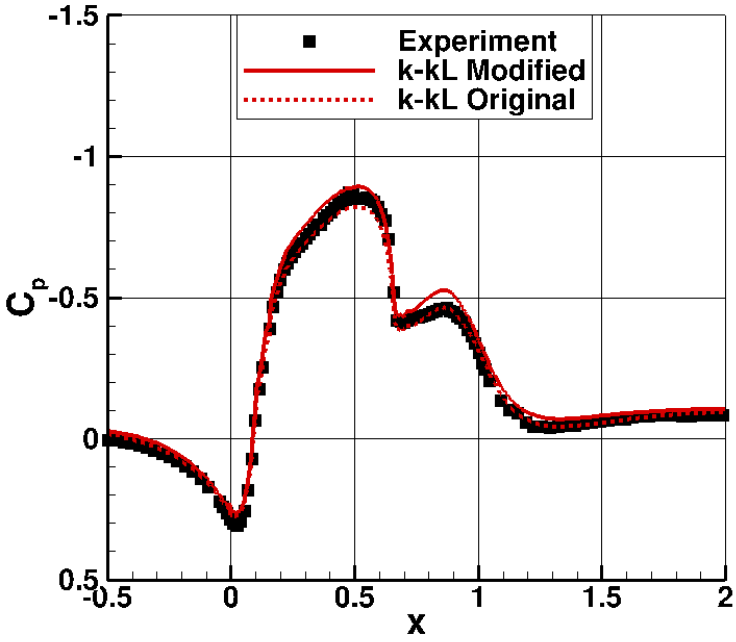

Figure 17 Surface pressure comparisons between experimental data and original and modified k-kL simulations for the hump model case.

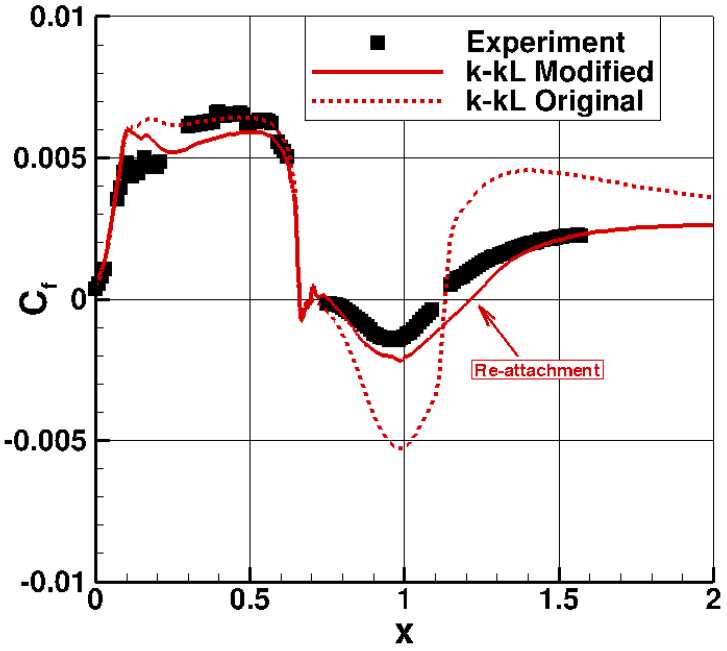

Figure 18 Skin friction comparisons between experimental data and original and modified k-kL simulations for the hump model case.

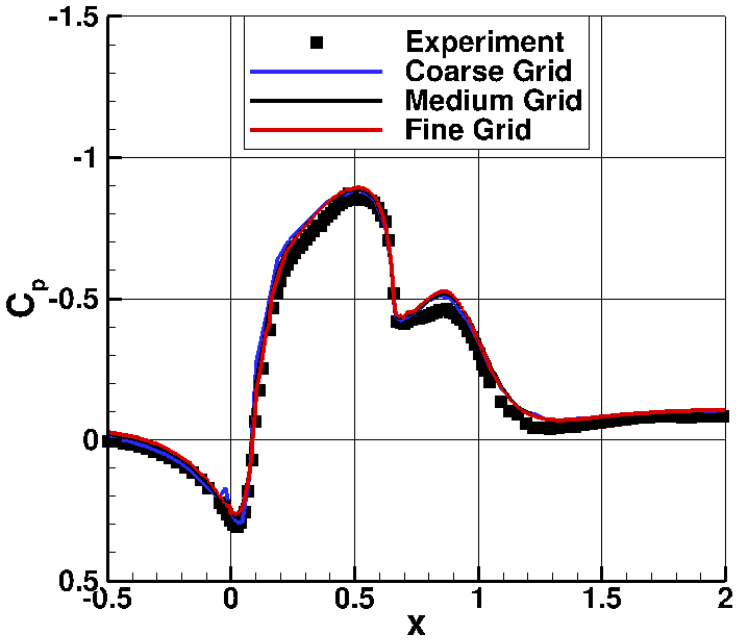

Figure 19 Surface pressure comparisons between experimental data and coarse, medium, and fine grid simulations for the hump model case.

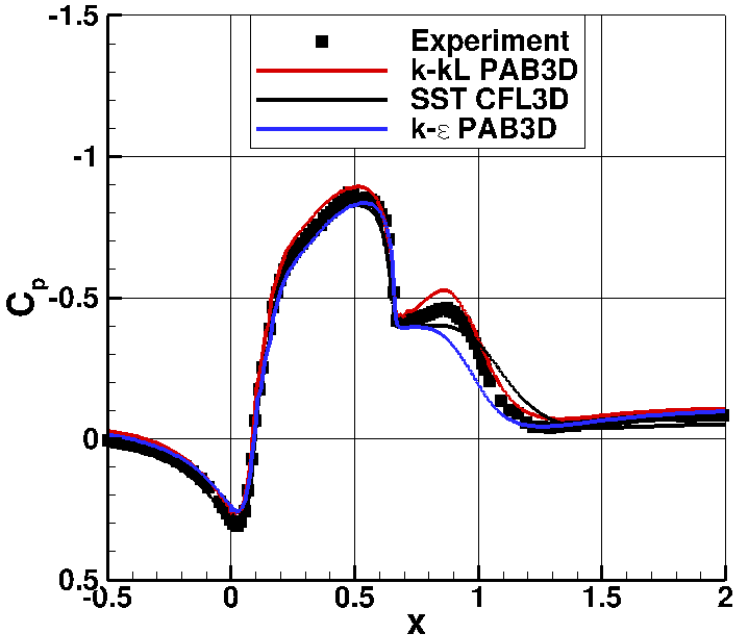

Figure 20 Surface pressure comparisons between experimental data and k-kL, SST, and k-e simulations for the hump model case.

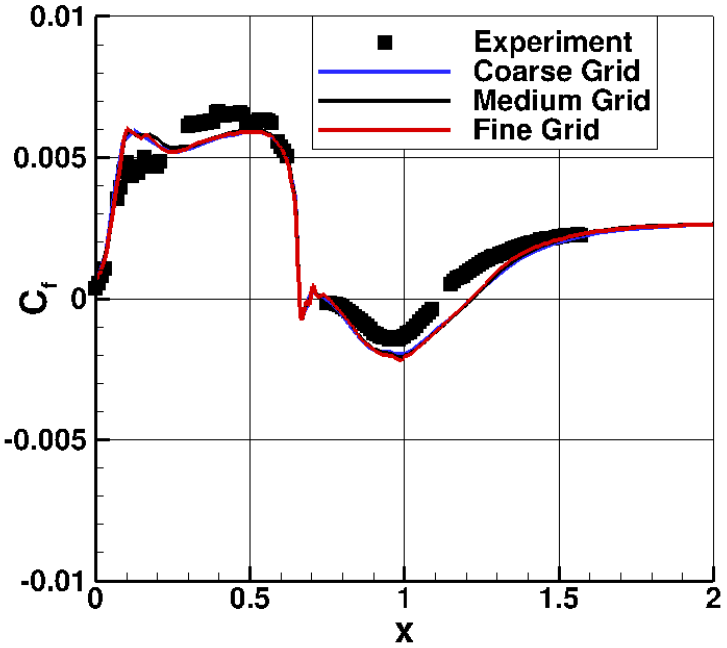

Figure 21 Skin friction comparisons between experimental data and coarse, medium, and fine grid simulations using k-kL model for the hump model case.

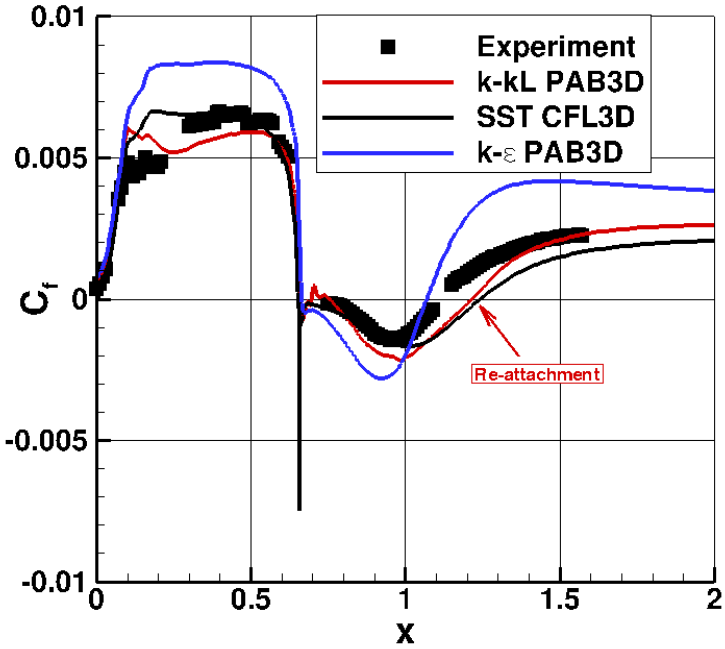

Figure 22 Skin friction comparisons between experimental data and k-kL, SST, and k-ε simulations for the hump model case.

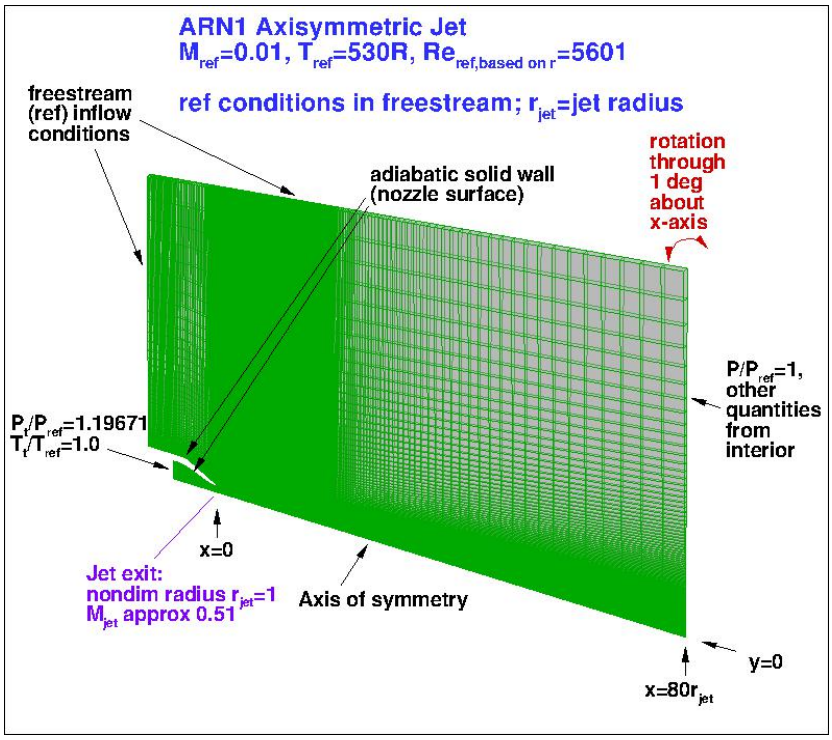

Figure 23 Grid distribution and flow conditions for subsonic jet flow case.

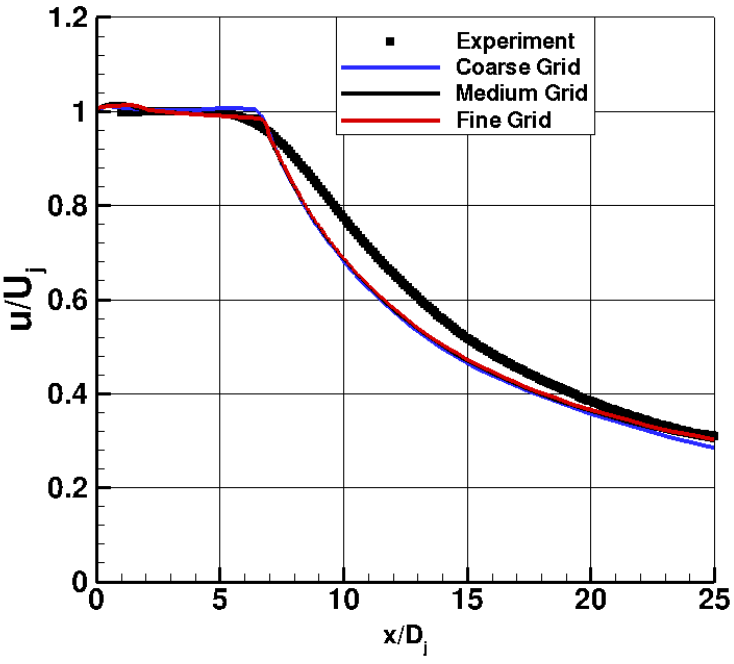

Figure 24 Grid effect on varations of centerline axial velocity using k-kL turbulence model for the jet flow case.

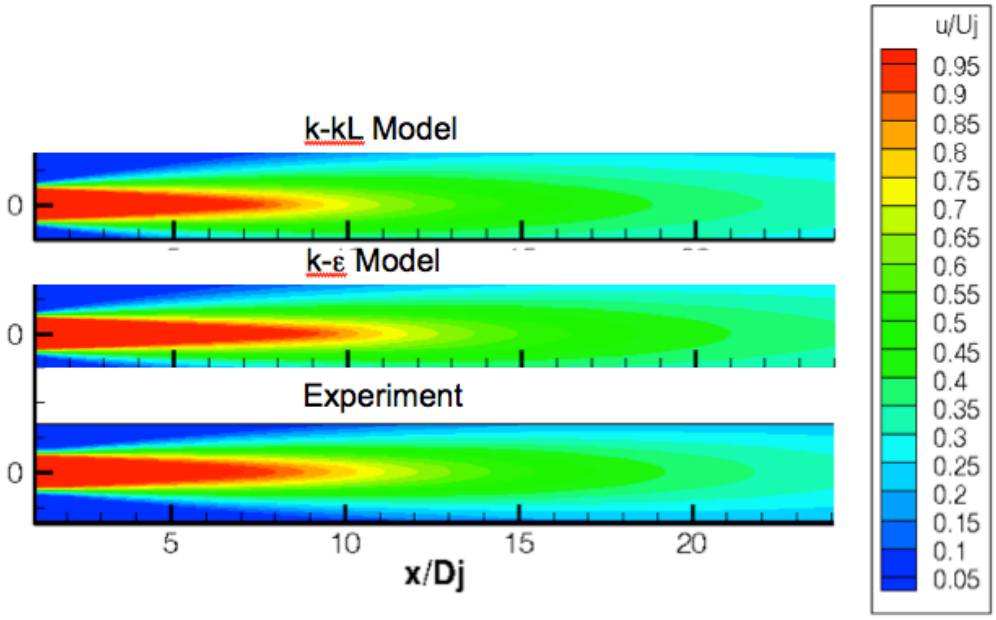

Figure 25 Normalized axial velocity comparisons between experimenal data and k-kL and k-ε turbulence models for the jet flow case.

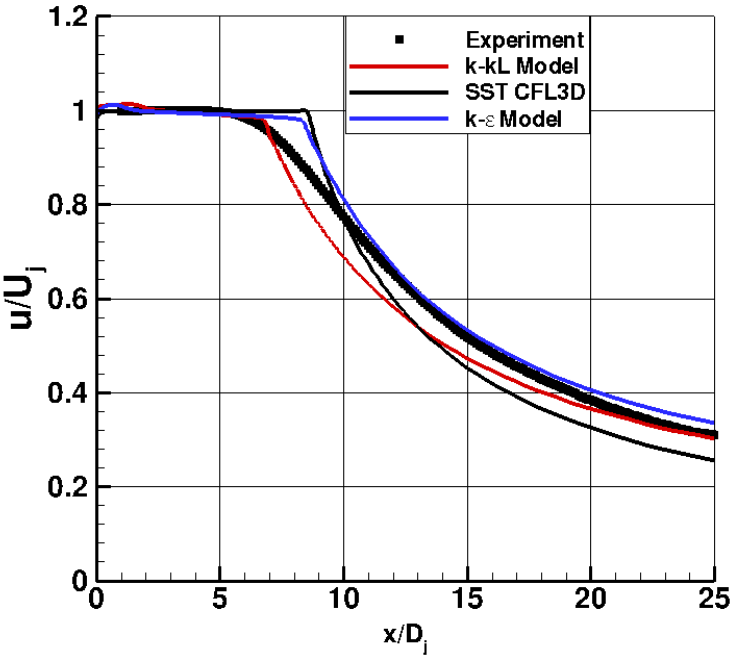

Figure 26 Axial centerline velocity comparisons between experimenal data and k-kL and k-ε turbulence models for the jet flow case.

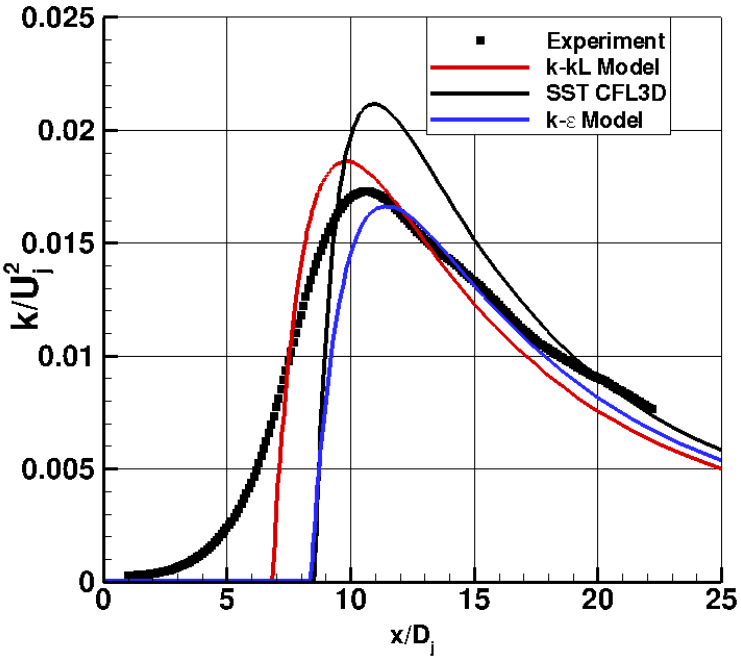

Figure 27 Turbulence kinetic energy comparisons between experimenal data and k-kL and k-ε turbulence models for the jet flow case.

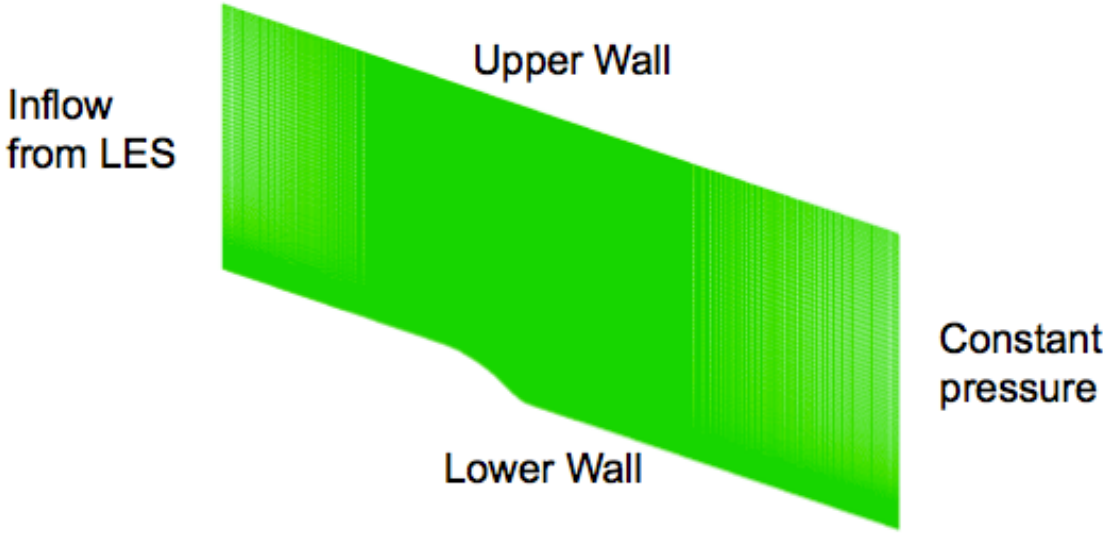

Figure 28 Grid distribution and flow conditions for 2D curved backward facing step.

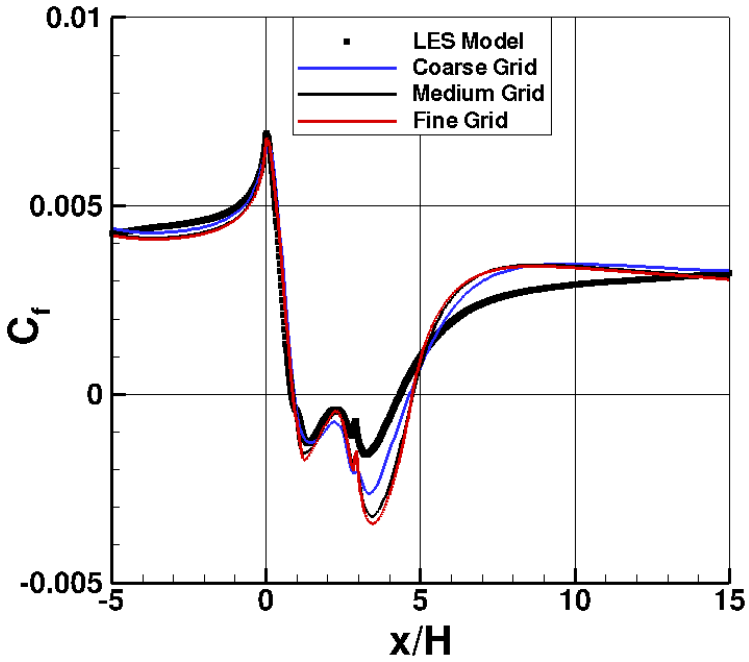

Figure 29 Skin friction comparisons between experimental data and coarse, medium, and fine grid simulations using k-kL model for the 2D curved backward facing step case.

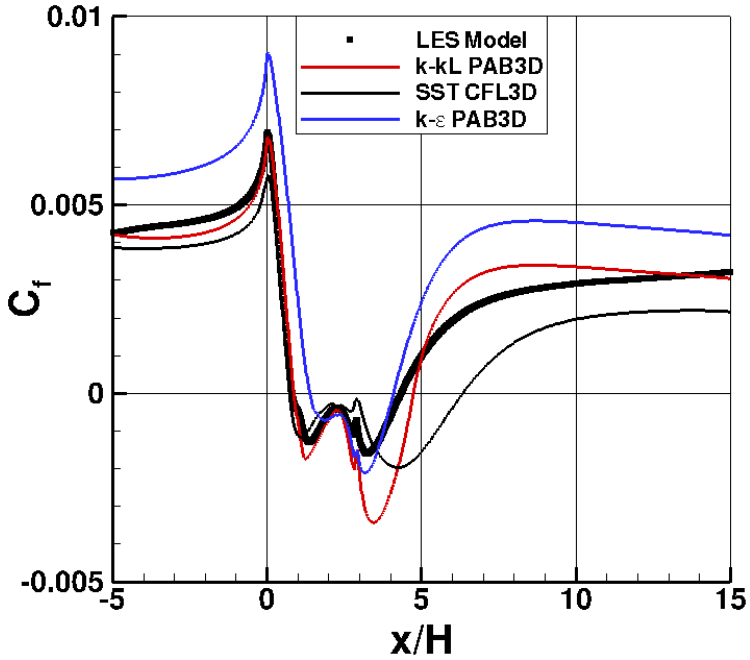

Figure 30 Skin friction comparisons between experimental data, and k-kL and k-e simulations for the 2D curved backward facing step case.

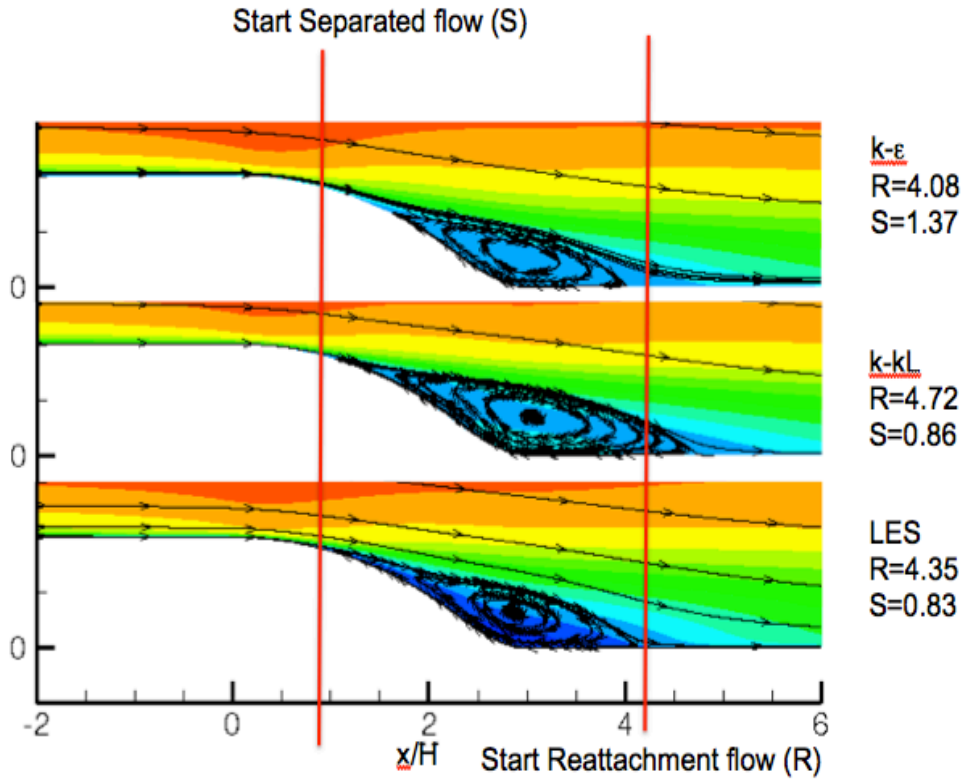

Figure 31 Comparison between LES and RANS turbulence models data separation and reattachment locations for the 2D curved backward facing step case.

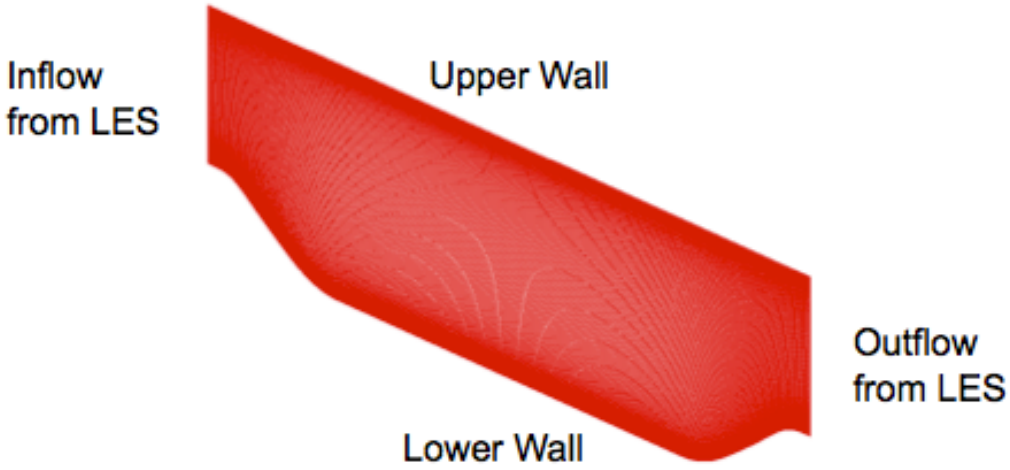

Figure 32 Grid distribution and boundary conditions for 2D periodic hill.

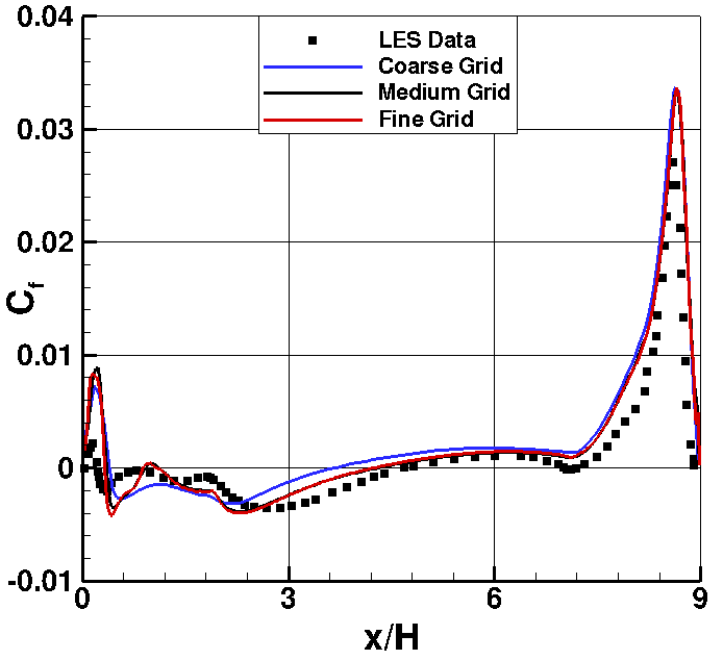

Figure 33 Skin friction comparisons between experimental data and coarse, medium, and fine grid simulations using k-kL model for the 2D periodic hill case.

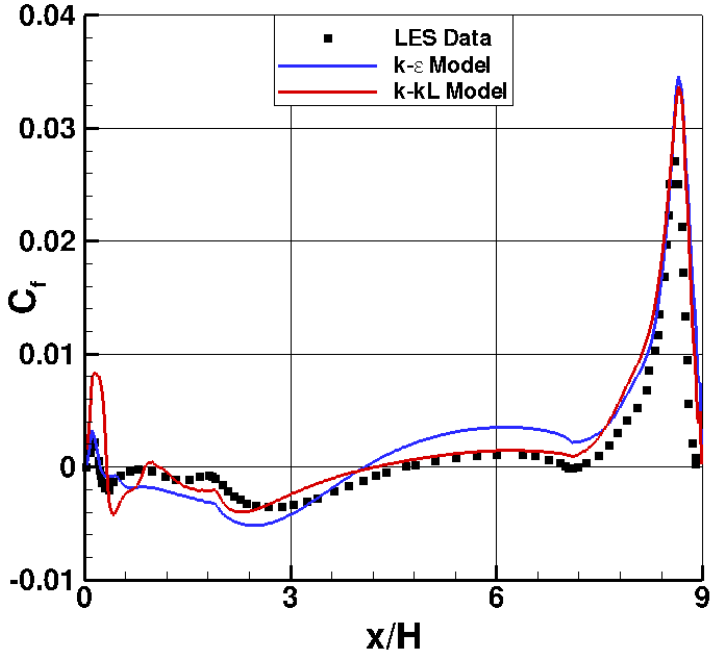

Figure 34 Skin friction comparisons between experimental data and k-kL, and k-ε simulations for the 2D periodic hill case.

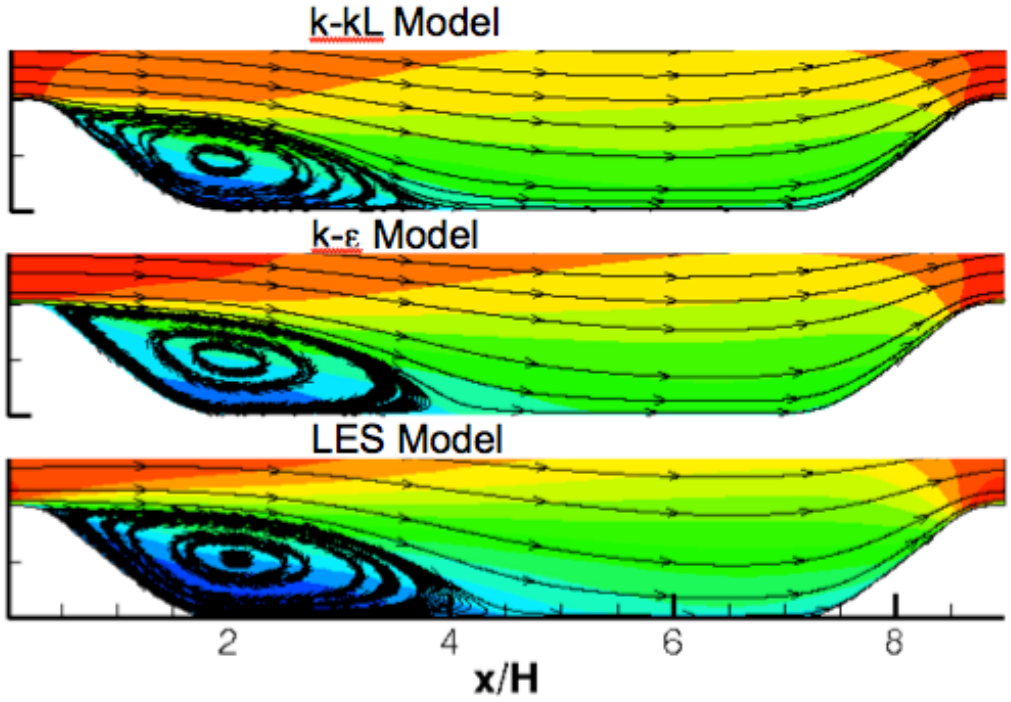

Figure 35 Comparison between LES and RANS turbulence model data separation and reattachment locations for the 2D periodic hill case.